



CrossMark  
click for updates

Cite this: *RSC Adv.*, 2015, 5, 1697

# Shaped-controlled synthesis of porous NiCo<sub>2</sub>O<sub>4</sub> with 1-3 dimensional hierarchical nanostructures for high-performance supercapacitors†

Ting Zhu,<sup>a</sup> En Rong Koo<sup>b</sup> and Ghim Wei Ho<sup>\*ab</sup>

Nickel/cobalt-based precursors (NCP) with 1-3 dimensional (1-3D) nanostructures were synthesized *via* a facile hydrothermal method. The as-prepared NCP were then transformed into porous NiCo<sub>2</sub>O<sub>4</sub> materials by calcination at 300 °C in air for 3 hours. The morphologies of the calcined samples retained a porous texture after calcination, where various 1-3D hierarchical nanostructures, including 2D nanobelts, interconnected 2D nanosheets forming a 3D structure, 1D nanoneedles assembled into chestnuts and 3D nanosponges, were formed. The as-derived structures were then evaluated as electrode materials for supercapacitors in virtue of their high surface areas (99–134 m<sup>2</sup> g<sup>-1</sup>). The results show that these porous NiCo<sub>2</sub>O<sub>4</sub> materials exhibited promising pseudo-capacitance with good cycling performance. The nanosponge sample registered the highest specific capacitance of 832 F g<sup>-1</sup> at a CV scan rate of 1 mV s<sup>-1</sup> due to its unique structure and highest surface area.

Received 8th November 2014  
Accepted 28th November 2014

DOI: 10.1039/c4ra14099k

[www.rsc.org/advances](http://www.rsc.org/advances)

## Introduction

Battery technology has been the widely preferred choice for energy storage applications in the last few decades, because of its high voltage limit, high energy density and sustainable power supply capability.<sup>1–3</sup> However, batteries have suffered from critical disadvantages such as shorter lifespan and safety issues, which have largely hindered their commercial market expansion, inspiring the industrial and research communities to hunt for alternative energy devices as back-up power supplies.<sup>4</sup> In recent years, supercapacitors have received intensive research interest due to their high power density, much longer cycle life and highly safe reliability as well as environmental friendliness.<sup>5–8</sup> As one of the most important building components of a supercapacitor device, electrode materials have been extensively focused on and studied, with the aim of fabricating novel electrodes for next generation high-performance supercapacitors.<sup>9–15</sup>

So far carbon materials such as conducting polymers and active carbon are widely used as electrode materials for supercapacitors fabrication owing to their low cost, excellent electric conductivity, good mechanical property and chemical stability.<sup>16,17</sup> However, these carbon based electrodes usually deliver very limited capacitance, hence restricting their practical

use in many fields.<sup>18,19</sup> Some recent emerging transitional metal oxide materials such as NiO, Co<sub>3</sub>O<sub>4</sub>, and MnO<sub>2</sub> are raising their importance as electrode materials as they can deliver very high specific capacitance due to their Faradic mechanism based redox reactions.<sup>20–28</sup> NiCo<sub>2</sub>O<sub>4</sub> is a low-cost binary metal oxide with good electronic conductivity and electrochemical activity than single component of nickel or cobalt oxide.<sup>29</sup> There have been several reports, demonstrating the synthesis and electrochemical measurements of nanostructured NiCo<sub>2</sub>O<sub>4</sub> materials.<sup>30–35</sup> For example, Lou and co-workers have employed a general solution method to grow mesoporous NiCo<sub>2</sub>O<sub>4</sub> nanosheets on different conductive substrates for supercapacitor electrodes.<sup>36</sup> Li *et al.* have reported the porous NiCo<sub>2</sub>O<sub>4</sub> nanowires, which exhibited a capacitance of 743 F g<sup>-1</sup> at a current density of 1 A g<sup>-1</sup>.<sup>37</sup> A very recent report by Dong *et al.* displayed the flower-like NiCo<sub>2</sub>O<sub>4</sub> nanostructures with high specific capacitance.<sup>38</sup> However, the material structure explorations based on a one-step synthesis that is tunable to produce 1D to 3D nanostructured materials and its relationship with the specific capacitance have not been well-explored. In this work, a simple and facile one-step synthesis is employed to prepare NCP with 1-3D hierarchical nanostructures. The morphologies of the as-prepared NCP are unique featuring distinctive building subunits. Then the as-derived NCP were then transformed into corresponding porous NiCo<sub>2</sub>O<sub>4</sub> materials by calcination at 300 °C in air for 3 hours. After calcination, the morphologies of the resultant NiCo<sub>2</sub>O<sub>4</sub> are well preserved, demonstrating various nanostructures including 2D nanobelts, interconnected 2D nanosheets forming a 3D structure, 1D nanoneedles assembled chestnuts and 3D nanosponges. In view of their unique structures and porous textures, the

<sup>a</sup>Department of Electrical and Computer Engineering, National University of Singapore, 4 Engineering Drive 3, 117576, Singapore. E-mail: [elehgw@nus.edu.sg](mailto:elehgw@nus.edu.sg)

<sup>b</sup>Engineering Science Programme, National University of Singapore, 4 Engineering Drive 3, 117576, Singapore

† Electronic supplementary information (ESI) available. See DOI: 10.1039/c4ra14099k

supercapacitor performances of the as-derived porous NiCo<sub>2</sub>O<sub>4</sub> materials have been evaluated and the 3D nanosponges exhibited the highest specific capacitance among all the samples.

## Experimental

### Materials preparations

All chemicals were of analytical grade and used as received without further purification. In a typical synthesis for preparing the NCP of 3D nanosponges, 0.1 g of urea, 0.5 g of Hexamethylenetetramine (HMT) and 0.1 g of cetyltrimethylammonium bromide (CTAB) were first dissolved in 30 mL of ethanol at 60 °C to obtain a clear solution. After that, 0.3 mL of Ni(NO<sub>3</sub>)<sub>2</sub> (0.1 M) and 0.6 mL of Co(NO<sub>3</sub>)<sub>2</sub> (0.1 M) were added into the solution before transferred to a Teflon-lined autoclave and heated in an air-flow oven at 140 °C for 12 hours. The resultant product was washed and centrifuged several times with DI water and ethanol before dried at 60 °C in an air-flow oven overnight. In order to obtain porous oxide materials, the dried precipitates were calcified at 300 °C for 3 hours under the atmosphere of air at a heating rate of 1 °C min<sup>-1</sup>. The matrices for preparing other NiCo<sub>2</sub>O<sub>4</sub> structures are described in Table 1.

### Materials characterization

The obtained samples are characterized by field-emission scanning electron microscopy (FESEM, JEOL FEG JSM-7001F) equipped with an energy dispersive X-ray spectroscopy (EDX), transmission electron microscopy (TEM, Philips FEG CM300 equipped with selected area electron diffraction (SAED)) and X-ray diffraction (XRD, Philips X-ray diffractometer, Cu K $\alpha$ ). The N<sub>2</sub> adsorption and desorption isotherms were measured at 77 K by a Quantachrome NOVA-1200 system. The BET surface area was calculated using adsorption data in a relative pressure ranging from 0.05 to 0.3.

### Electrochemical measurements

The working electrodes were prepared by mixing the 80 wt% of electroactive material (NiCo<sub>2</sub>O<sub>4</sub>), 10 wt% of carbon black, and 10 wt% of polyvinylidene difluoride (PVDF, Aldrich). The slurry was then pressed onto metal Ni foams, and dried thoroughly at 60 °C. The electrolyte used was a 2 M of KOH aqueous solution. The electrochemical performances of the samples were evaluated on a CHI 660D electrochemical workstation using cyclic voltammetry and chronopotentiometry tests with a three-electrode cell where Pt foil serves as the counter electrode and a standard calomel electrode (SCE) as the reference electrode.

## Results and discussion

Table 1 shows the experimental conditions for the NCP synthesis. The NCP of nanobelts and interconnected nanosheets were prepared using HMT as precipitator, whose calcined NiCo<sub>2</sub>O<sub>4</sub> products are marked as Sample I and II respectively, while the NCP of nanochestnuts and nanosponges were synthesized using urea as precipitator, whose resultant NiCo<sub>2</sub>O<sub>4</sub> have been marked as Sample III and IV, respectively. The formation mechanisms of all the NCP products are very complicated due to the introduction of various precipitators and surfactants. The added HMT or urea or CTAB may have been served as soft templates for the formation of NCP during the hydrothermal process. However, the solvent also played an important role in this process, since the product by pure ethanol (Sample IV) is totally different from those obtained in pure water (Sample I–III).

Morphologies of all the NCP products were examined by FESEM (Fig. 1). The 2D very thin nanobelts show an average length of 2–5  $\mu$ m with a width of 2  $\mu$ m (Fig. 1a). Fig. 1b displays an FESEM image of the interconnected nanosheets, which have been formed into micro-sized 3D assembly. 0.1 g of urea instead of HMT has led to the chestnut-like particles, which are composed of ultralong (>2  $\mu$ m) nanoneedles (Fig. 1c). It is interesting to observe that the morphology is changed to be nanosponge when 0.5 g of HMT and 0.1 g of CTAB were introduced into the synthesis based on the chestnut-like recipe (Fig. 1d). The crystallographic structures for all the four NCP samples have been checked by XRD (Fig. S1†), and the obtained

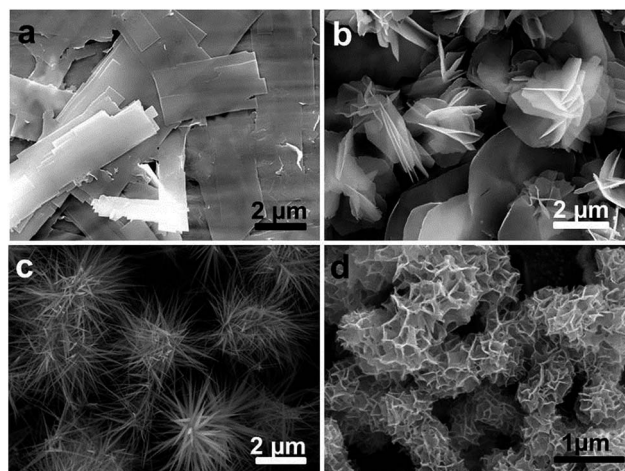


Fig. 1 FESEM images of the NCP Sample I (a), II (b), III (c) and IV (D).

Table 1 Synthetic illustration of the various morphologies

Morphologies	Ni(NO <sub>3</sub> ) <sub>2</sub> (mL)	Co(NO <sub>3</sub> ) <sub>2</sub> (mL)	Urea (g)	HMT (g)	CTAB (g)	Solvent (30 mL)
Nano-belts	0.3	0.6	0	1	0	DI water
Interconnected nano-sheets	0.3	0.6	0	0.1	0	DI water
Nano-chestnuts	0.3	0.6	0.1	0	0	DI water
Nano-sponges	0.3	0.6	0.1	0.5	0.1	Ethanol

patterns show that all the four samples are in poor crystallinity, and it is speculated that they are mixture of  $\text{Ni}(\text{OH})_2$  and  $\text{Co}(\text{OH})_2$  after comparing with the standard XRD patterns of  $\text{Ni}(\text{OH})_2$  and  $\text{Co}(\text{OH})_2$ .

The as-formed NCPs were calcined into  $\text{NiCo}_2\text{O}_4$  samples at  $300^\circ\text{C}$  in air for 3 h, and their FESEM results are displayed in Fig. 2. Some of the belts (Sample I) were seen to be broken after calcination, which may be due to their thin 2D structures (Fig. 2a). The general profile of nanosheets assembly (Sample II) is preserved, which can be observed from Fig. 2b. The chest-nut like particles (Sample III) also show good thermal stability as the overall structure is intact and no broken nanoneedles were observed (Fig. 2c and d). The heat treatment has made the nanosponges (Sample IV) more connected with one another which can be seen from Fig. 2e. In addition, a higher magnification FESEM image shows that the calcination process has led the structure to be more porous (Fig. 2f).

Due to their hierarchical structures and thermal stability, the Sample III and IV were further analyzed by TEM and their results are illustrated in Fig. 3. The nanoneedles of Sample III are shown to be cone-like rods with a length over 500 nm (Fig. 3a). Fig. 3b shows a high resolution TEM (HR-TEM) image which is taken from the area indicated by the red circle in Fig. 3a. The detected crystal lattice with a spacing of 0.24 nm can be attributed to the (311) of  $\text{NiCo}_2\text{O}_4$ .<sup>39</sup> For Sample IV, The 3D structure of nanosponges has been well retained after calcination, which can be confirmed again by TEM result shown in Fig. 3c. The further detailed TEM image in Fig. 3d reveals that the nanosponges are assembled by ultrathin nanosheets with highly porous texture, which may be due to the removal of organic species during the

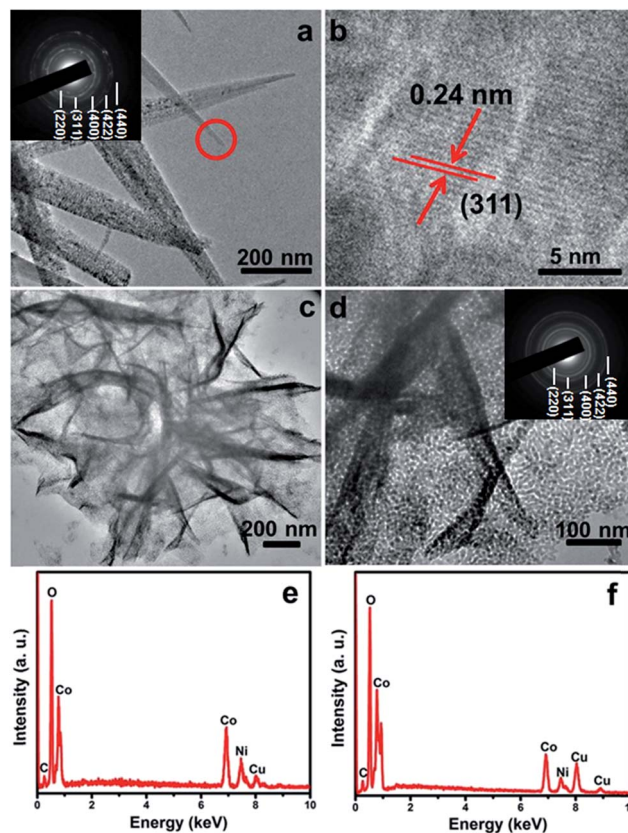


Fig. 3 TEM (a, c and d), HR-TEM (b), SAED patterns (insets in a and d) and EDX (e and f) of the as-derived  $\text{NiCo}_2\text{O}_4$  Sample III (a, b and e) and IV (c, d and f).

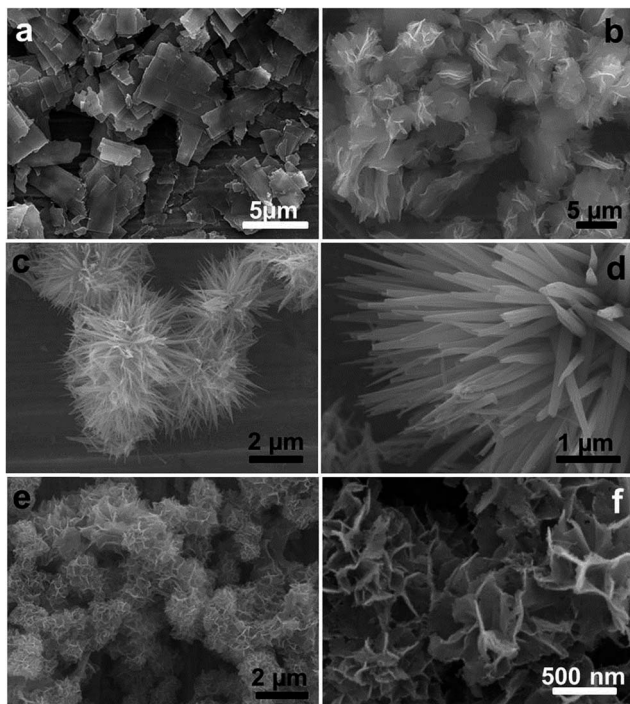


Fig. 2 FESEM images of the as-derived  $\text{NiCo}_2\text{O}_4$  Sample I (a), II (b), III (c and d) and IV (e and f).

combustion. The further SAED patterns shown in the insets of Fig. 3a and d reveal that both Sample III and IV are in polymorph due to their circular structures, and their corresponding lattice planes have been indicated in Fig. 3a and d insets. The EDX results performed on Cu substrate for Sample III and IV are shown in Fig. 3e and f, respectively. Strong peaks of Ni, Co and O can be detected for both of the samples, indicating the formation of nickel cobalt oxide.

The crystallographic phases of all the as-obtained  $\text{NiCo}_2\text{O}_4$  samples were examined by XRD (Fig. 4). After comparing with the standard pattern, All the indexed peaks were attributed to (220), (311), (400), (422), (511) and (440) planes, which can be assigned to be cubic  $\text{NiCo}_2\text{O}_4$  (JCPDS 73-1702).<sup>40</sup> As such, there are no signs of impurities and thus has assured that the synthesis was successful in creating pure  $\text{NiCo}_2\text{O}_4$  of the respective morphologies.

The re-crystallization of NCP and removal of organic species may occur during the combustion, which could endow the resultant  $\text{NiCo}_2\text{O}_4$  materials with porous texture. BET measurements were performed at 77 K to investigate the textural characteristics of all the four samples.  $\text{N}_2$  adsorption-desorption isotherms of Sample I–IV are shown in Fig. 5 with insets illustrating their corresponding pore size distributions obtained from respective desorption branches. These isotherms can be categorized as type IV with small hysteresis loops

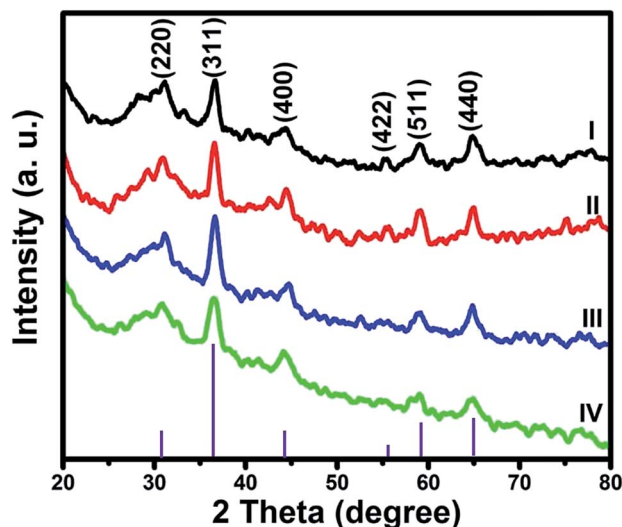


Fig. 4 XRD patterns of the as-derived Sample I–IV, respectively.

observed at a relative pressure of 0.3–0.9 for Sample I, II and III, and 0.8–1.0 for Sample IV. The BET specific surface areas are determined to be 99, 91.3, 116 and 134  $\text{m}^2 \text{g}^{-1}$  for Sample I, II, III and IV, respectively, which has shown all the four samples relatively high porosity. It can be concluded from the pore size distribution that Sample I, II and III have pores with diameter around 2 nm, while Sample IV possesses a larger pore size at 4–6 nm. Furthermore, Sample IV has shown a multiple pore size distribution compared to the other three samples, revealing its wide range of pore sizes that may be accessible for different sizes of hydrated electrolyte ions.<sup>41</sup>

In virtue of the unique structures and high surface areas, the as-derived  $\text{NiCo}_2\text{O}_4$  porous materials were evaluated as electrodes for supercapacitors. The redox reactions involved during the charge and discharge process can be described as follows:<sup>42</sup>

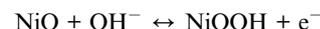


Fig. 6 shows the CV curves obtained with different scan rates (1–20  $\text{mV s}^{-1}$ ) from a voltage window of 0–0.6 V (*vs.* SCE) for Sample I, III and IV, and an optimized window of 0–0.5 V (*vs.* SCE) for Sample II. It can be clearly observed that there are two pairs of peaks (but only one broad and combined peak can be seen at higher scan rates) associated with the Faradaic redox reactions related to M–O/M–O–OH, where M refers to Ni or Co.<sup>43,44</sup> For Sample I, III and IV, the two pairs of redox peaks are located within 0.25–0.4 V and 0.4–0.6 V, respectively. Different from the other samples, the redox peaks of Sample II appear within 0.15–0.3 V and 0.3–0.4 V, which can be observed from Fig. 6b. The average specific capacitance of the four samples can be calculated from the CV curves based on the following equation:<sup>45</sup>

$$C = \frac{1}{mu(V_2 - V_1)} \int_{V_1}^{V_2} I(V)dV$$

where  $I$  (A) is the current,  $m$  (g) is the mass of the active material,  $u$  ( $\text{V s}^{-1}$ ) is the scan rate,  $V_1$  and  $V_2$  are the voltage cuts during the CV scanning.

The average specific capacitances of the respective samples calculated from various scan rates are presented in Fig. 7.

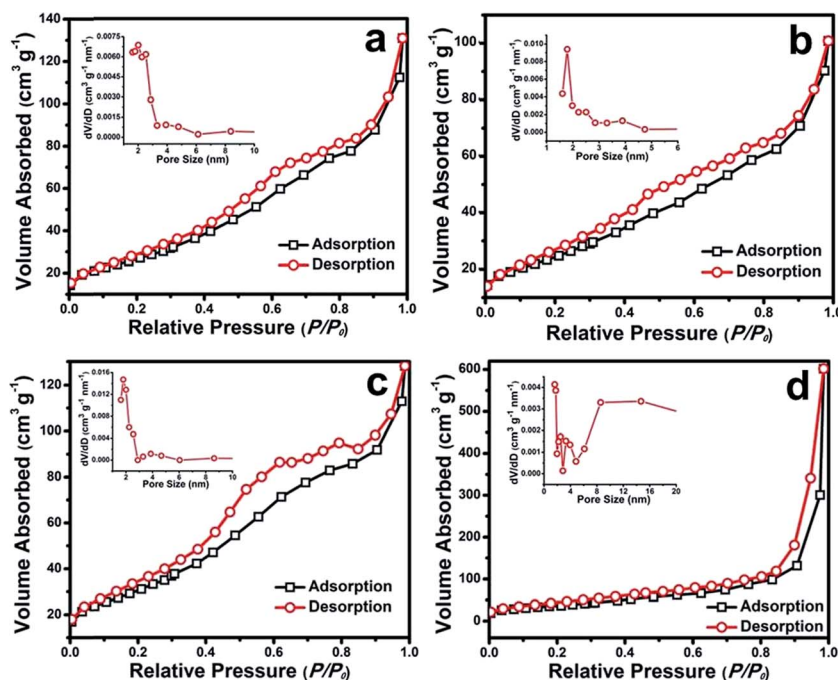


Fig. 5 BET results of the as-derived Sample I (a), II (b), III (c) and IV (d), respectively.

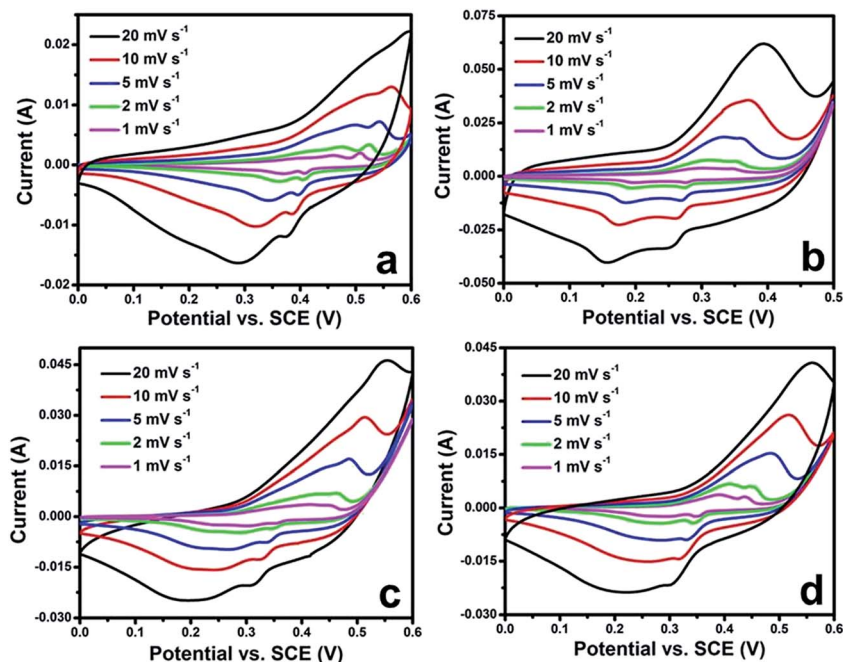


Fig. 6 CV curves of the as-derived Sample I (a), II (b), III (c) and IV (d), respectively.

Specific capacitances of 238, 232, 220, 202, and 162  $\text{F g}^{-1}$  can be delivered at scan rates of 1, 2, 5, 10, and 20  $\text{mV s}^{-1}$  for Sample I. While for Sample II, higher capacitances of 315, 298, 281, 270, and 252  $\text{F g}^{-1}$  can be obtained with the same CV scan rates, exhibiting that the 3D interconnected nanosheets show better performance than the nanobelts. Compared to Sample I and II, Sample III and IV show higher capacitances of 675  $\text{F g}^{-1}$  and 832  $\text{F g}^{-1}$  respectively at 1  $\text{mV s}^{-1}$ , which is comparable to a previous work reported by Hu *et al.*, where 764  $\text{F g}^{-1}$  was reported for their porous  $\text{NiCo}_2\text{O}_4$ .<sup>46</sup> In this work, even at a higher scan rate (20  $\text{mV s}^{-1}$ ), specific capacitances of 384  $\text{F g}^{-1}$  for Sample III and 493  $\text{F g}^{-1}$  for Sample IV can be calculated, both of which are much higher than the maximum values of Sample I and II. The

high capacitances of Sample III and IV may be due to their higher surface areas (BET results in Fig. 5) than the Sample I and II. In addition, the 2D nanobelts and 3D interconnected nanosheets are more bulky and compact compared to the other two samples, which may have made it more difficult for the electrolyte ions to diffuse into the inner areas of the particles, hence reducing the specific capacitance of the materials.

For the same electrodes, the galvanostatic constant-current charge–discharge measurements are also conducted at various current densities to present the respective capacitance, which has been demonstrated in Fig. 8. Samples I, III and IV are tested at 2, 5, 10 and 20  $\text{A g}^{-1}$  with a voltage range between 0 to 0.5 V (vs. SCE), while Sample II is tested at same current densities within an optimized voltage window (0–0.45 V vs. SCE).

The specific capacitances of all the four samples calculated from the different current densities are presented in Fig. 9. It can be seen from the curves that Sample IV (nanosponge) has delivered the highest capacitance of 792  $\text{F g}^{-1}$  at a current density of 2  $\text{A g}^{-1}$ , which is much higher than those of Sample I (200  $\text{F g}^{-1}$ ) and II (288  $\text{F g}^{-1}$ ) calculated at the same current density. This value is also higher than a work by Yang *et al.*, where 658  $\text{F g}^{-1}$  at 1  $\text{A g}^{-1}$  was reported for their  $\text{NiCo}_2\text{O}_4$  nanostructures.<sup>42</sup>

Consistent with the results of CV curves, the Sample III (nanochestnuts) shows the second best performance among the four samples, which has delivered high capacitances of 712–280  $\text{F g}^{-1}$  at current densities from 2 to 20  $\text{A g}^{-1}$ , respectively. It is also interesting to note that 392  $\text{F g}^{-1}$  can be retained even at a high current density (20  $\text{A g}^{-1}$ ) for the Sample IV, whose value is even higher than those of Sample I and II obtained from the lowest current density (2  $\text{A g}^{-1}$ ), indicating the excellent performance of the nanosponge sample. Furthermore, the higher capacitances of Sample III and IV than those of Sample I

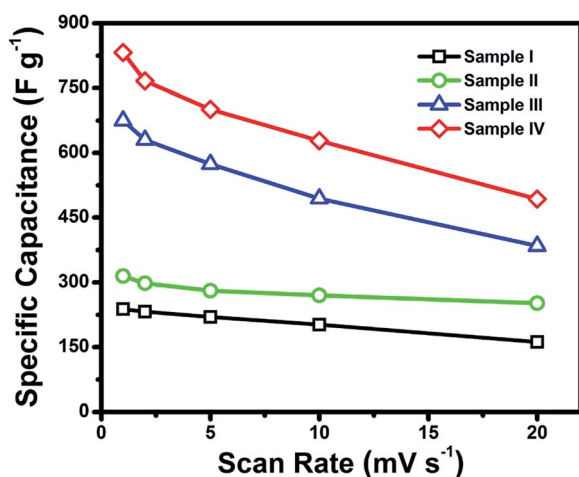


Fig. 7 Specific capacitances calculated from CV curves of the as-derived Sample I–IV, respectively.

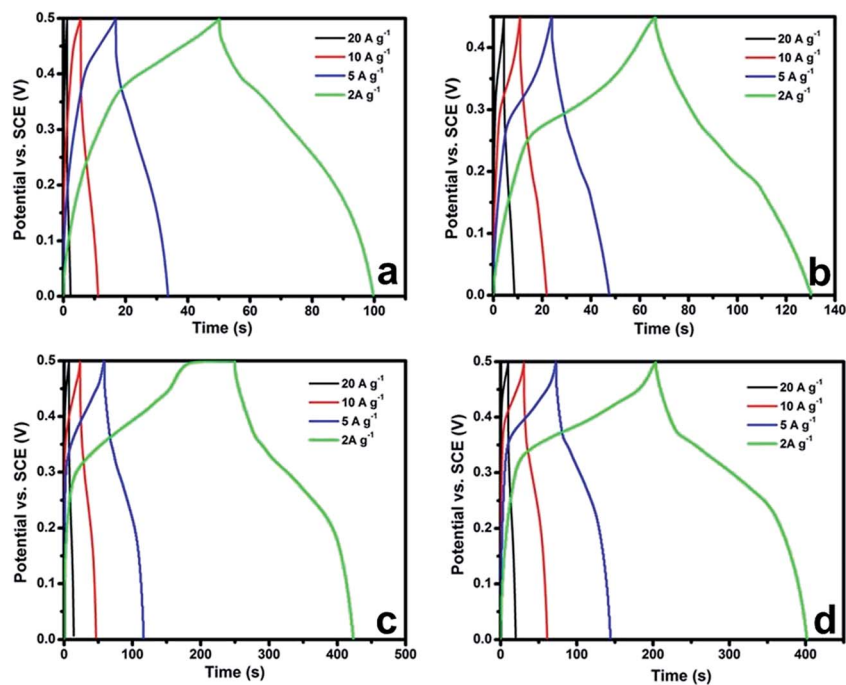


Fig. 8 Charge–discharge curves of Sample I (a), II (b), III (c) and IV (d) at different current densities.

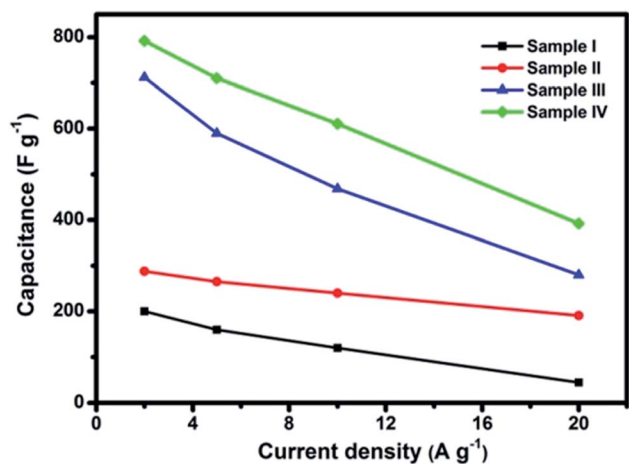


Fig. 9 Specific capacitances of Sample I–IV calculated from different current densities.

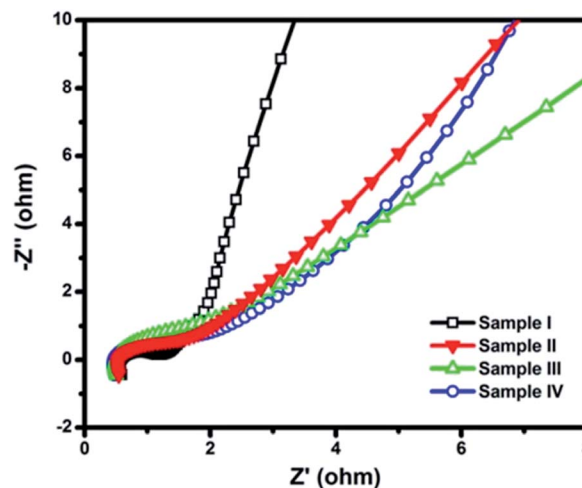


Fig. 10 EIS results of the as-derived Sample I–IV, respectively.

and II can also be revealed by the EIS results (Fig. 10), where smaller semicircles of Sample I and II can be observed, suggesting their better conductivity.

The cycling stability is very important for supercapacitors, and hence prolonged cycles have been performed at  $10 \text{ mV s}^{-1}$  for all the four samples. Fig. 11 displays the cycling performances for Sample I–IV, respectively. After 1000 cycles, there is no distinct capacitance decay for Sample I–IV, which shows their good cyclic stabilities upon the cycling process. It is interesting to note that a capacitance increase can be observed at the first 300 cycles for Sample IV. This increase may be attributed to the high porosity of ultrathin nanosheets of

Sample IV (as seen from the TEM result in Fig. 3d). The large surface area will allow the electrolyte ions to diffuse into the interiors *via* different sizes of the pore channels, which would show an electrode activation process.<sup>23</sup> Among all the four samples, the 3D nanosponges have shown the best performance, which may be due to its unique sponge-like structures with the highest surface area ( $134 \text{ m}^2 \text{ g}^{-1}$ ), providing the materials with more electroactive sites for the redox reactions.<sup>47,48</sup> Also, It should be indicated that the pure Ni foam only contributed  $\sim 1.2\%$  of the total capacitance of the sponge sample, showing the most of the capacitances are delivered by the electroactive materials.

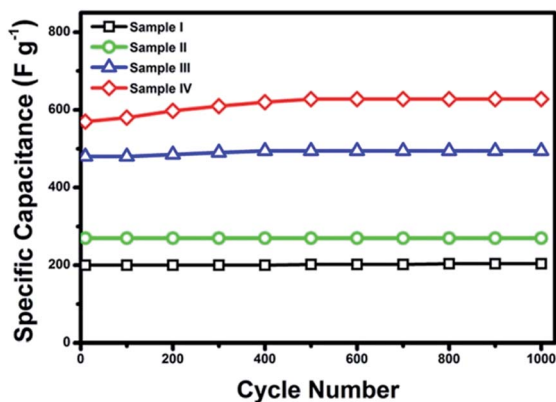


Fig. 11 Cycling performances of the as-derived Sample I–IV, respectively.

## Conclusions

In summary, we have prepared NCP products with various morphologies by a facile one-pot hydrothermal method. The as-formed NCP were transformed to  $\text{NiCo}_2\text{O}_4$  samples *via* calcination at 300 °C in air for 3 h. The morphologies of the calcined  $\text{NiCo}_2\text{O}_4$  products were well preserved after calcination, showing their good thermal stability. All the  $\text{NiCo}_2\text{O}_4$  materials have shown to be in porous texture holding high BET surface areas from 91–134  $\text{m}^2 \text{g}^{-1}$ . The as-derived porous  $\text{NiCo}_2\text{O}_4$  were then evaluated as electrode materials for supercapacitors. The specific capacitances calculated from CV curves have shown that the 3D nanospheres exhibited the best performance with a highest capacitance of 832  $\text{F g}^{-1}$  at a CV scan rate of 1  $\text{mV s}^{-1}$ . In addition, all the four samples have delivered good cycling performances till 1000 cycles, which show their potential use for next-generation high-performance supercapacitors.

## Acknowledgements

This work was financially supported by MOE R-263-000-653/654-731/112.

## References

- B. Kang and G. Ceder, *Nature*, 2009, **458**, 190–193.
- J. M. Tarascon and M. Armand, *Nature*, 2001, **414**, 359–367.
- K. S. Kang, Y. S. Meng, J. Breger, C. P. Grey and G. Ceder, *Science*, 2006, **311**, 977–980.
- P. Poizot, S. Laruelle, S. Grugeon, L. Dupont and J. M. Tarascon, *Nature*, 2000, **407**, 496–499.
- Y. W. Zhu, S. Murali, M. D. Stoller, K. J. Ganesh, W. W. Cai, P. J. Ferreira, A. Pirkle, R. M. Wallace, K. A. Cychoz, M. Thommes, D. Su, E. A. Stach and R. S. Ruoff, *Science*, 2011, **332**, 1537–1541.
- P. Simon and Y. Gogotsi, *Nat. Mater.*, 2008, **7**, 845–854.
- A. S. Arico, P. Bruce, B. Scrosati, J. M. Tarascon and W. Van Schalkwijk, *Nat. Mater.*, 2005, **4**, 366–377.
- M. Winter and R. J. Brodd, *Chem. Rev.*, 2004, **104**, 4245–4269.
- B. Zhao, J. S. Song, P. Liu, W. W. Xu, T. Fang, Z. Jiao, H. J. Zhang and Y. Jiang, *J. Mater. Chem.*, 2011, **21**, 18792–18798.
- C. Liu, F. Li, L. P. Ma and H. M. Cheng, *Adv. Mater.*, 2010, **22**, E28–E62.
- Z. Chen, V. Augustyn, J. Wen, Y. W. Zhang, M. Q. Shen, B. Dunn and Y. F. Lu, *Adv. Mater.*, 2011, **23**, 791–795.
- C. Z. Yuan, L. Yang, L. R. Hou, L. F. Shen, F. Zhang, D. K. Li and X. G. Zhang, *J. Mater. Chem.*, 2011, **21**, 18183–18185.
- W. F. Wei, X. W. Cui, W. X. Chen and D. G. Ivey, *Chem. Soc. Rev.*, 2011, **40**, 1697–1721.
- H. L. Wang, H. S. Casalongue, Y. Y. Liang and H. J. Dai, *J. Am. Chem. Soc.*, 2010, **132**, 7472–7477.
- F. Shi, L. Li, X. L. Wang, C. D. Gu and J. P. Tu, *RSC Adv.*, 2014, **4**, 41910–41921.
- L. L. Zhang and X. S. Zhao, *Chem. Soc. Rev.*, 2009, **38**, 2520–2531.
- J. Lee, J. Kim and T. Hyeon, *Adv. Mater.*, 2006, **18**, 2073–2094.
- G. P. Wang, L. Zhang and J. J. Zhang, *Chem. Soc. Rev.*, 2012, **41**, 797–828.
- X. Xiao, X. Peng, H. Y. Jin, T. Q. Li, C. C. Zhang, B. Gao, B. Hu, K. F. Huo and J. Zhou, *Adv. Mater.*, 2013, **25**, 5091–5097.
- C. Z. Yuan, X. G. Zhang, L. H. Su, B. Gao and L. F. Shen, *J. Mater. Chem.*, 2009, **19**, 5772–5777.
- F. Jiao, A. H. Hill, A. Harrison, A. Berko, A. V. Chadwick and P. G. Bruce, *J. Am. Chem. Soc.*, 2008, **130**, 5262–5266.
- S. J. Ding, T. Zhu, J. S. Chen, Z. Y. Wang, C. L. Yuan and X. W. Lou, *J. Mater. Chem.*, 2011, **21**, 6602–6606.
- T. Zhu, J. S. Chen and X. W. Lou, *J. Mater. Chem.*, 2010, **20**, 7015–7020.
- S. K. Meher and G. R. Rao, *J. Phys. Chem. C*, 2011, **115**, 15646–15654.
- J. P. Liu, J. Jiang, M. Bosman and H. J. Fan, *J. Mater. Chem.*, 2012, **22**, 2419–2426.
- L. Yang, S. Cheng, Y. Ding, X. B. Zhu, Z. L. Wang and M. L. Liu, *Nano Lett.*, 2012, **12**, 321–325.
- Z. P. Li, Y. J. Mi, X. H. Liu, S. Liu, S. R. Yang and J. Q. Wang, *J. Mater. Chem.*, 2011, **21**, 14706–14711.
- M. K. Liu, W. W. Tjui, J. S. Pan, C. Zhang, W. Gao and T. X. Liu, *Nanoscale*, 2014, **6**, 4233–4242.
- G. Q. Zhang, H. B. Wu, H. E. Hoster, M. B. Chan-Park and X. W. Lou, *Energy Environ. Sci.*, 2012, **5**, 9453–9456.
- L. F. Shen, Q. Che, H. S. Li and X. G. Zhang, *Adv. Funct. Mater.*, 2014, **24**, 2630–2637.
- J. F. Li, S. L. Xiong, Y. R. Liu, Z. C. Ju and Y. T. Qian, *ACS Appl. Mater. Interfaces*, 2013, **5**, 981–988.
- D. Zhang, H. Yan, Y. Lu, K. Qiu, C. Wang, Y. Zhang, X. Liu, J. Luo and Y. Luo, *Dalton Trans.*, 2014, 15887–15897.
- X. Y. Yao, C. Y. Zhao, J. H. Kong, D. Zhou and X. H. Lu, *RSC Adv.*, 2014, **4**, 37928–37933.
- Z. Y. Wang, Y. F. Zhang, Y. H. Li and H. Y. Fu, *RSC Adv.*, 2014, **4**, 20234–20238.
- X. Y. Liu, S. J. Shi, Q. Q. Xiong, L. Li, Y. J. Zhang, H. Tang, C. D. Gu, X. L. Wang and J. P. Tu, *ACS Appl. Mater. Interfaces*, 2013, **5**, 8790–8795.
- G. Q. Zhang and X. W. Lou, *Adv. Mater.*, 2013, **25**, 976–979.

- 37 H. Jiang, J. Ma and C. Z. Li, *Chem. Commun.*, 2012, **48**, 4465–4467.
- 38 Y. F. Zhang, M. Z. Ma, J. Yang, H. Q. Su, W. Huang and X. C. Dong, *Nanoscale*, 2014, **6**, 4303–4308.
- 39 Q. F. Wang, B. Liu, X. F. Wang, S. H. Ran, L. M. Wang, D. Chen and G. Z. Shen, *J. Mater. Chem.*, 2012, **22**, 21647–21653.
- 40 L. L. Li, Y. Cheah, Y. W. Ko, P. Teh, G. Wee, C. L. Wong, S. J. Peng and M. Srinivasan, *J. Mater. Chem. A*, 2013, **1**, 10935–10941.
- 41 C. Largeot, C. Portet, J. Chmiola, P. L. Taberna, Y. Gogotsi and P. Simon, *J. Am. Chem. Soc.*, 2008, **130**, 2730–2731.
- 42 J. W. Xiao and S. H. Yang, *RSC Adv.*, 2011, **1**, 588–595.
- 43 H. L. Wang, Q. M. Gao and L. Jiang, *Small*, 2011, **7**, 2454–2459.
- 44 T. Y. Wei, C. H. Chen, H. C. Chien, S. Y. Lu and C. C. Hu, *Adv. Mater.*, 2010, **22**, 347–351.
- 45 C. H. An, Y. J. Wang, Y. A. Huang, Y. A. Xu, C. C. Xu, L. F. Jiao and H. T. Yuan, *CrystEngComm*, 2014, **16**, 385–392.
- 46 C. T. Hsu and C. C. Hu, *J. Power Sources*, 2013, **242**, 662–671.
- 47 T. Zhu, Z. Y. Wang, S. J. Ding, J. S. Chen and X. W. Lou, *RSC Adv.*, 2011, **1**, 397–400.
- 48 H. B. Wu, H. Pang and X. W. Lou, *Energy Environ. Sci.*, 2013, **6**, 3619–3626.